ADVANCED OPTICAL MATERIALS
www.advopticalmat.de

Crystallization Regulation and Defect Passivation of High-Performance Flexible Perovskite Light-Emitting Diodes Based on Novel Dielectric/Metal/Dielectric Transparent Electrodes

Kai Sun, Zhiqiang Bao, Xiaoyang Guo, Deyue Zou, Ying Lv, Jingqiu Liang,* and Xingyuan Liu**

Perovskite materials are considered as potential materials suitable for flexible wearable displays due to their excellent optoelectronic properties and flexibility. However, the brittleness of conventional ITO electrodes, as well as the poor crystallization of perovskite on flexible substrates, have hindered the development in flexible perovskite light-emitting diodes (PeLEDs). Herein, a flexible PeLED based on a novel transparent electrode WO_3/Au/WO_3 (WAW), combined with the adjustment method of incorporation of polymer [polyethylene oxide-polypropylene oxide-polyethylene oxide triblock copolymer (P123)], is proposed to assist crystallization and defect passivation. The strong anchoring effect between P123 and perovskite accelerates the nucleation and crystallization process of perovskite films based on flexible substrates (shortened from 10 min to 1 min), induces the formation of uniform and small-sized perovskite grains, and passivates non-radiation defects caused by poor crystal quality. As a result, a high-performance green PeLED with a maximum external quantum efficiency (EQE) of 14.45% is obtained. The corresponding flexible PeLED displays a maximum EQE of 11.9%, and it can keep a 96.5% original current efficiency after bending for 1000 cycles. This work will provide feasible guidance for the design and manufacture of high-performance flexible all-inorganic PeLEDs.

1. Introduction

With the development of science and technology, the demand for flexibility, wearable, and portable optoelectronic products is increasing, which has become one of the important trends of the development of optoelectronic products in the future.[1–3] Recently, as a new type of semiconductor material, perovskite materials have excellent optoelectronic properties such as high carrier mobility, high fluorescence quantum efficiency, long lifetime, adjustable band gap, high color purity, wide color gamut, and easy processing, exhibiting great application potential in the next generation lighting and displays.[4–8] Moreover, perovskite materials possess good flexibility and ductility, which could be attributed to the high degree of anisotropy, low shear modulus, and low mechanical hardness of perovskite crystals.[9] So perovskite materials have also been regarded as potential materials suitable for flexible lighting, wearable displays, and biomedical devices.[10–12]

Although the efficiency of perovskite light-emitting diodes (PeLEDs) has been greatly improved, the performance of flexible PeLEDs is still far behind and remains one of the main challenges.[13] In order to meet the practical application requirements of flexible devices, each functional layer of flexible PeLEDs should have outstanding mechanical properties such as good flexibility and bending stability, especially transparent electrodes,[14–17] and perovskite emission layers.[18–20] However, the high-temperature preparation process, limited Indium (In) element content, and inherent brittleness of traditional Indium tin oxide (ITO) electrode lead to poor bending resistance and incompatibility with the flexible substrate, resulting in the degradation of optoelectronic performance of flexible PeLEDs.[21–24] The use of new electrodes to replace ITO electrodes has become one of the main strategies, such as AZO,[25] graphene,[26] metal foil,[27] and silver nanowires.[28] These strategies have improved the bending stability of the electrodes to a certain extent, but there are still some problems, such as poor device stability, complicated preparation process, poor conductivity, and poor adhesion.[29–34]

K. Sun, Z. Bao, X. Guo, D. Zou, Y. Lv, J. Liang, X. Liu
State Key Laboratory of Luminescence and Applications
Changchun Institute of Optics
Fine Mechanics and Physics, Chinese Academy of Sciences
Changchun 130033, P. R. China
E-mail: guoxy@ciomp.ac.cn; liangjq@ciomp.ac.cn; liuxy@ciomp.ac.cn
K. Sun, Z. Bao, D. Zou
University of Chinese Academy of Sciences
Beijing 100049, P. R. China
J. Liang
Key Laboratory of Optical System Advanced Manufacturing
Changchun Institute of Optics
Fine Mechanics and Physics, Chinese Academy of Sciences
Changchun 130033, P. R. China

The ORCID identification number(s) for the author(s) of this article can be found under https://doi.org/10.1002/adom.202301752

DOI: 10.1002/adom.202301752

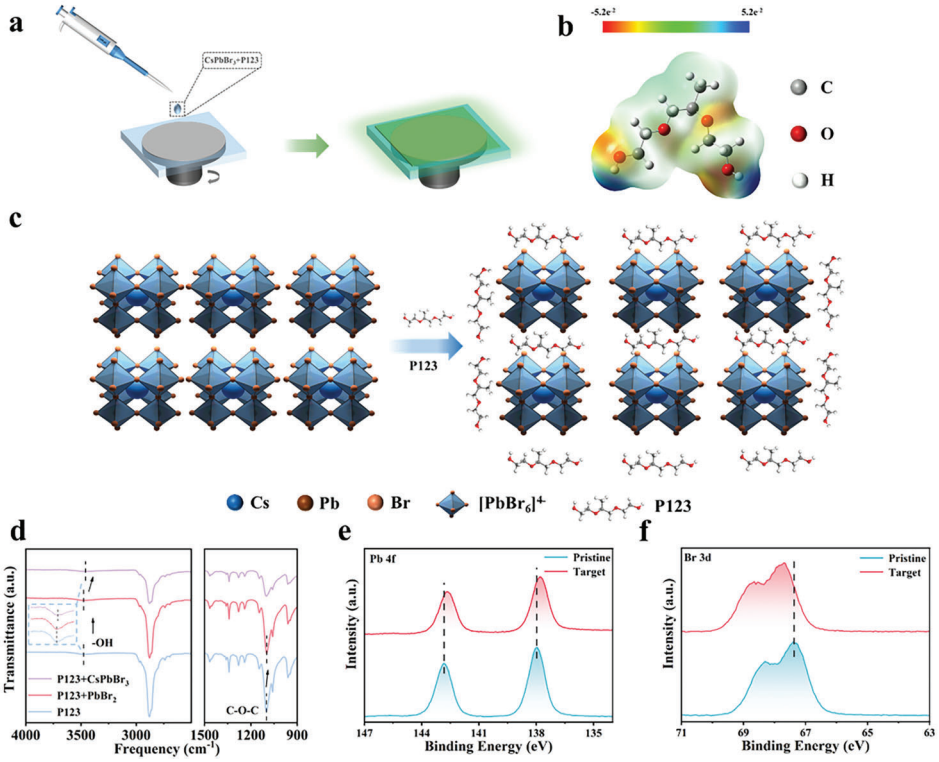

Figure 1. Passivation of $CsPbBr_3$ perovskite film. a) Schematic preparation process of the perovskite film with P123 additive. b) ESP configuration of the P123. c) Schematic of perovskite modification. d) FTIR spectra of pure P123, P123/$PbBr_2$, and $CsPbBr_3$ mixture. e,f) XPS spectra of e) Pb 4f, f) Br 3d core levels from the pristine and target perovskite films.

The dielectric/metal/dielectric (DMD) electrode has the advantages of various structural components, adjustable properties, and resistance to bending. The optical and electrical properties of DMD electrodes can be adjusted by the choice of dielectric and metal layers. During the past few years, it has been widely applied in flexible and transparent optoelectronic devices, such as flexible organic[35] and quantum light-emitting diodes,[36] flexible and semitransparent photovoltaics,[37] and so on. In recent years, DMD transparent electrodes have also been used as the top transparent electrodes to realize transparent PeLEDs.[38–40] However, the DMD electrode has seldom been used in the field of flexible PeLEDs. On the other hand, the surface morphology and grain size distribution of perovskite films will significantly affect the optoelectronic and mechanical performance of flexible PeLEDs. Feasible strategies such as additive engineering,[41] morphology control,[42] and material composition management[6] have been successfully demonstrated in rigid PeLEDs, but their application in flexible PeLEDs is still lacking in research. Therefore, the development of transparent electrodes and perovskite films with excellent optoelectronic properties and high mechanical stability is essential to realize efficient, stable, and flexible PeLEDs.

In this work, a new WO_3/Au/WO_3 (WAW) transparent electrode is used as the bottom electrode of PeLED, and the additive polyethylene oxide-polypropylene oxide-polyethylene oxide triblock copolymer (P123) is introduced to optimize the crystallization kinetics and recombination kinetics of the perovskite films. The optimized green PeLED achieves a maximum luminance of 10 200 cd m^{-2}, peak current efficiency (CE) of 42.4 cd A^{-1}, and an EQE of 14.45%. At the same time, the maximum luminance, peak CE, and maximum EQE of the PeLED on flexible substrate are 3390 cd m^{-2}, 39.2 cd A^{-1}, and 11.9%, respectively. After being folded 1000 times under a bending radius of 4.45 mm, the CE of the flexible device can maintain 96.5% of its original value, proving good bending stability.

2. Results and Discussion

We introduced the polymer P123 into the 3D all-inorganic perovskite system to realize the preparation of flexible perovskite films. As shown in **Figure 1**a, the perovskite precursor solution of $CsPbBr_3$+P123 was spin-coated onto PEDOT:PSS/WAW-based electrodes by a one-step spin-coating technique, and the detailed experimental information is shown in the experimental section. In order to improve the transmittance while ensuring the continuity and conductivity of the metal layer, the optoelectronic performance of the WAW electrode were optimized by changing the thicknesses of Au (Figure S1, Supporting Information). When the thickness of Au reached 8 nm, the transmittance and square resistance of WAW electrode are 73% and 9 Ω sq^{-1}, respectively (Table S1, Supporting Information), the best figure of merit (FoM) is obtained. Therefore, we used the optimized WAW as the flexible electrode substrate, and denoted "pristine" and "target" to denote the unmodified and P123-modified perovskite films, respectively.

To maximize the photophysical properties of the green-emitted perovskite film, the additive P123 was then introduced into the

perovskite precursor for defecting passivation. We employed density functional theory (DFT) to calculate the electrostatic potential (ESP) distribution of the P123 molecule to assess its defect passivation capacity as seen in Figure 1b. O atom is located at ether group (C–O–C) and hydroxyl group (–OH) functional moiety, shows distinct electronegativity, indicative of high electron density, which can combine with the uncoordinated Pb^{2+} ions, and forms hydrogen bonds with the Br^- ions in perovskite, respectively.[1] Therefore, we portray the supposed interactions between P123 and $CsPbBr_3$ perovskite in Figure 1c. Halide vacancies accompanied by uncoordinated lead defects on the surface of the bare perovskite act as the nonradiative recombination centers, leading to inferior PLQY, while P123 molecules as Lewis bases provide lone pair electrons and passivate unsaturated Pb^{2+}.[43,44]

To further confirm the interaction between P123 and perovskite through experiment, the Fourier-transform infrared (FTIR) spectroscopy was performed. Figure 1d shows the FTIR spectra of P123 and its mixtures with $PbBr_2$ and $CsPbBr_3$, respectively. With the appearance of $PbBr_2$, the stretching vibration peak of the C–O–C functional group in P123 shifted to a lower wavenumber (from 1100 to 1097 cm^{-1}), indicating that the C–O–C bond is weakened. However, the stretching vibration peak of the -OH functional group of P123 has not changed, indicating that the -OH bond and single $PbBr_2$ have almost no effect. With the emergence of the 3D structure of $CsPbBr_3$, the -OH functional group moved to a lower wavenumber (from 3475 to 3460 cm^{-1}), which indicated that the interaction between –OH and perovskite resulted in a weakened binding force.[45–48] Furthermore, the X-ray photoelectron spectroscopy (XPS) of pristine and target films was detected and analyzed, as shown in Figure 1e,f, and Table S2 (Supporting Information). The O 1s core level representing C–O in the target perovskite film exhibits a lower binding energy compared to P123 powder. The distinctive peaks of Pb $4f_{5/2}$ and $4f_{7/2}$ clearly shift to low binding energy after P123 treatment. In contrast, the core level of Br 3d shifts to a high binding energy. We attribute the variation in the FTIR and XPS spectra to the contribution of the lone-pair electrons on the oxygen atom of the C–O functional group to the empty 6p orbital of Pb^{2+}, and the formation of hydrogen bonds between –OH and Br^- within the octahedral framework $[PbBr_6]^{4-}$.[49] Taking into account the above results, we deduce that P123 acts as an efficient crystal cross-linker in the perovskite structures through a strong anchoring effect of both coordination bonds and hydrogen bonds, thus accelerating the nucleation and crystallization process, and passivates the surface defects of perovskite.

The interaction between additives and perovskite affects the nucleation and crystallization processes of perovskite. The nucleation stage usually occurs rapidly during the spin-coating process, and the crystallization of the perovskite film is gradually completed during the annealing process. Therefore, in order to understand how the polymeric additive regulates the crystallinity process of perovskite, we explored the UV–vis absorption spectrum during the annealing process as shown in **Figure 2**a,b and Figure S3a,b (Supporting Information). With the increase of annealing time, the exciton absorption peak at 500–520 nm of the pristine perovskite film shifts gradually. While the target perovskite film showed a stable absorption peak after annealing for 1 min, indicating a faster crystallization process.[50] Steady-state fluorescence spectra (Figure 2c,d and Figure S3c,d (Supporting Information)) show that as the annealing time increases, the pristine perovskite film changed from a complicated multimodal co-luminescence phenomenon to a uniform luminescence phenomenon, indicating that the perovskite crystals transitioned from a solvent-mixed semi-crystalline state to a fully crystalline state. In Figure 2d, the target film exhibited stable and uniform luminescence peaks only after annealing for 1 min, indicating that the strong anchoring effect of the P123 polymer effectively stabilized the crystal structure and accelerated the crystallization process. This strong anchoring effect can be attributed to the hydrogen bonding between -OH and Br^- and the coordination of C–O with Pb^{2+}, as confirmed by the FTIR and XPS measurements discussed above.[50–52] During annealing process, the interaction between P123 and $CsPbBr_3$ improves the crystallization kinetics of perovskite and shortens the cycle time of the preparation process.

To further investigate the effect of different annealing times on pristine and target perovskite crystals, we performed X-ray diffraction (XRD) characterizations. As shown in Figure S4 (Supporting Information), the signal intensity of the diffraction peaks gradually increased, indicating that the annealing time directly affected the crystallization kinetics of perovskite. Subsequently, the corresponding films were characterized by atomic force microscopy (AFM). As shown in Figure S5 (Supporting Information), under the condition of annealing for 1 min, the perovskite surface can be clearly observed in an incompletely crystallized state in the pristine perovskite film, and a partially incomplete crystal phase is present. However, the target perovskite film is in a fully crystalline state, the small crystal grains on the surface of the film are uniform and dense, and the incomplete crystal phase disappears. With the increase of annealing time, the crystals on the pristine film surface gradually completed crystallization, while the target film surface showed grain growth and grain boundaries formation. A large number of grain boundaries often cause non-radiative defects and affect the radiative recombination efficiency, so as to adjust the annealing time to modulate the crystalline morphology. In Figure 2e,f, it can be found that the optimal annealing condition is 1 min, and the target perovskite film at this time has a more uniform grain distribution, a smaller grain size (Dave ≈ 55.75 nm), and a lower roughness (Rq = 3.5 nm), which are conducive to the formation of high-quality perovskite films for efficient PeLEDs.

The reason for the accelerated crystallization was further elucidated by contact angle measurements (Figure S6, Supporting Information). The contact angles of the pristine and target perovskite solutions on PEDOT:PSS are 33.5° and 19.5°, respectively. According to the nucleation theory, the free energy (ΔG) required for crystal nucleation and the contact angle (θ) have the following relationship:[19]

$$\Delta G_{heterogenous} = \Delta G_{homogenous} \times f(\theta) \quad (1)$$

$$f(\theta) = \frac{1}{4}(1 - \cos\theta)^2 \times (2 + \cos\theta) \quad (2)$$

where $\Delta G_{heterogenous}$ and $\Delta G_{homogenous}$ represent the free energy required for heterogeneous nucleation and homogeneous nucleation, respectively. It can be seen from the formula that the

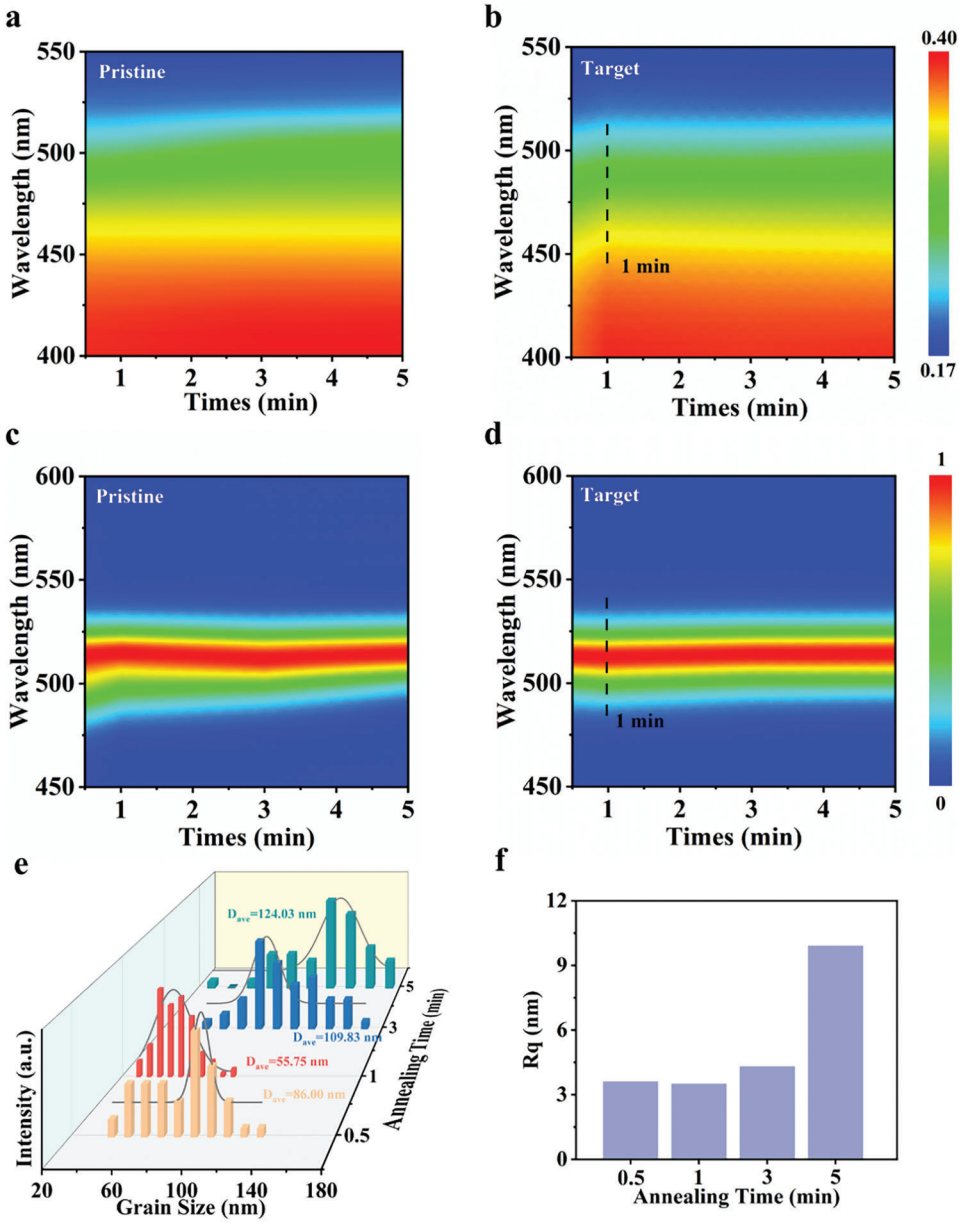

Figure 2. Spectral and morphological characterization of the pristine and target perovskite films. a,b) Absorption, c,d) PL spectra of perovskite films, and e) Grains size distribution and f) Rq statistics of target perovskite films during the annealing process at 70 °C.

reduction of the contact angle θ will lead to a decrease of $f(\theta)$, thereby reducing the free energy required for nucleation, which is more conducive to crystal nucleation. According to the results, it is known that the perovskite film can nucleate and grow more easily with the addition of P123. Therefore, the target film has a faster crystallization rate, higher crystalline quality, and lower non-radiative defects than those of the pristine film, which contribute to the enhancement of the electroluminescence (EL) efficiency and flexibility of PeLEDs.

To gain insight into the photophysical effects of pristine and target thin films, UV–vis absorption and photoluminescence (PL) spectra were performed to study the optical properties of pristine and target films. As shown in **Figure 3**a, relative to the absorption peak (505 nm) of pristine sample, the absorption peak of target film shifted to 500 nm. Meanwhile, compared with pristine film, the PL peak of target film had a slight blue shift from 520 to 516 nm, and its FWHM increased from 18.8 to 19.6 nm, which could be attributed to the P123 induced small-sized grain formation and passivation of surface defects in perovskite.[53–55] To investigate the effect of P123 on the $CsPbBr_3$ exciton recombination process, the time-resolved PL (TRPL) spectra of pristine and target perovskite films were measured, as shown in Figure 3b. TRPL curves were fitted by a triple-exponential decay function,[56] and the fitting parameters are summarized in Table S2 (Supporting Information). Among them, τ_1 is the fast process of non-radiative recombination, τ_2 is the process of bi-

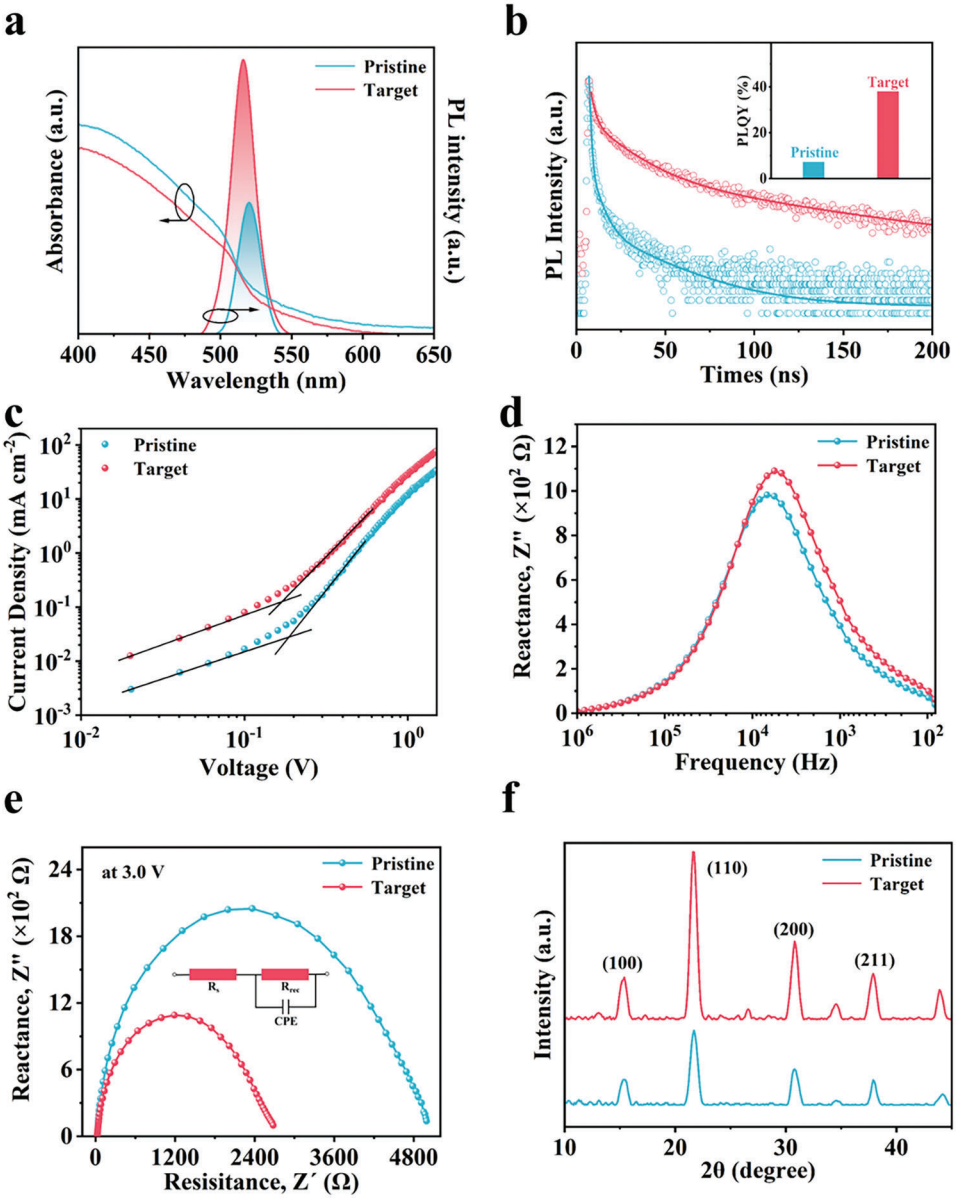

Figure 3. Properties of perovskite films and devices. a) UV–Vis absorption and PL spectra. b) time-resolved PL spectra and the inset shows the PLQYs of perovskite films. c) SCLC data. d) Reactance Z''-frequency curves of PeLED. e) Impedance spectra of PeLEDs at a DC bias of 3.0 V. The inset is the equivalent circuit model. f) XRD patterns of pristine and target perovskite films.

molecular radiative recombination, and τ_3 is the slow process of radiative recombination. Thus, A_1, A_2, and A_3 are the fractions of fast (τ_1), medium (τ_2), and slow (τ_3) decaying components, respectively. The target perovskite film shows a high ratio of radiative to non-radiative recombination, and the average lifetime is extended from 7.5 to 55.6 ns. Therefore, the photoluminescence quantum yield (PLQY) of the perovskite film was significantly increased from 7% to 38% after P123 modification. This suggests that P123 can suppress non-radiative recombination in perovskite and make photogenerated excitons more inclined to radiative recombination, thus increasing the PLQY of $CsPbBr_3$, which again confirms that there are decreased surface defects in target thin films.[57] To further verify the reduction of trap states in the target film, the space charge limited current (SCLC) method was performed (Figure 3c). The current density-voltage (J–V) curves of the hole-only devices constructed by WO_3/ Au/ WO_3 / PEDOT: PSS/ $CsPbBr_3$/ MoO_3/ Al were measured under the dark condition. The formula for calculating defect density is as follows:[58]

$$N_{defects} = \frac{2\epsilon_0\epsilon_r V_{TFL}}{qL^2} \quad (3)$$

ϵ_r and ϵ_0 are the dielectric constant and the vacuum permittivity, q is the electron charge, L refers to the thickness of the perovskite

film, and V_{TFL} is the transition voltage. Thereinto, ϵ_r and C can be expressed as:[59]

$$\epsilon_r = \frac{CL}{\epsilon_0 S} \tag{4}$$

$$C = -\frac{1}{2\pi F Z''} \tag{5}$$

where C is the geometrical capacitance, S represents the area of the film, Z'' is the imaginary part of impedance, and F is frequency. According to the impedance imaginary part-frequency (Z''–F) curve (Figure 3d), the target can hardly change the C value of the perovskite film in the high-frequency region. In the low-frequency region, the C of target device is obviously smaller than the pristine device. Therefore, the lower V_{TFL} and C obtained in target film imply a lower concentration of trap states in the perovskite film.[60] The TRPL and SCLC results demonstrate that the defects of perovskite films can be effectively passivated and non-radiative recombination can be reduced by applying P123 modification. Considering the apparent morphological evolution of perovskite film by using P123, impedance spectroscopy (IS) measurement was then implemented for normally working PeLED to study their charge transport and recombination characteristics (Figure 3e). When both the devices are driven under the same bias, the arc radius in Nyquist plot of the target device is much smaller than that of the pristine one. This variation reveals the significantly reduced charge-transfer resistance, which can be expected to be favorable for enhancing the EL performance of PeLED. We speculate that the improved electrical properties may be attributed to compact and uniform small-size grains assembled in the target films. In Figure 3f, the prepared pristine and target films representing the peak positions of (100), (110), (200), and (211) crystal planes did not change significantly, but the intensity of the diffraction peaks increased significantly. This indicates that the addition of P123 does not cause changes in the crystal structure of $CsPbBr_3$, but improves the crystallinity of perovskite film, which is conducive to improving the efficiency and luminance of PeLEDs.[61]

To further investigate the effect of P123 on the perovskite film, the temperature-dependent PL spectroscopy was used to explain the change of excitons in the perovskite film (Figure S7, Supporting Information). As temperature increases, the luminescence peaks of the two perovskite films show a similar trend, the intensity of the luminescence peak becomes weaker, the spectrum appears blue-shifted, and the FWHM increases. We attribute the effect of thermal expansion of the lattice. In order to further study the exciton binding energy (E_b) of the perovskite film, the integrated intensity of the variable temperature PL peak was fitted by the Arrhenius equation:[62]

$$I(T) = \frac{I_0}{1 + Ae^{\frac{-E_b}{k_B T}}} \tag{6}$$

where I_0 and k_B are the PL intensity and Boltzmann constant at 0 K, respectively. According to the fitting results, the E_b of pristine and target perovskite films are 54.8 and 126.5 meV, respectively. The temperature-dependent PL spectroscopy results confirmed that the introduction of P123 can increase the E_b of perovskite films and enhance their luminescent properties.

Encouraged by these excellent optical properties, green PeLED with the structure of WAW/PEDOT:PSS/$CsPbBr_3$/TPBi/LiF/Al were fabricated (**Figure 4**a). Each functional layer of the device can be clearly seen from the SEM image (Figure S8a, Supporting Information). Compared with the widely used ITO electrode (−4.7 eV), the WAW electrode has a higher work function (−5.2 eV), which better matches the energy level of PEDOT:PSS (−5.1 eV), which is conducive to hole injection, thereby improving the charge injection efficiency of the device (Figure S8b, Supporting Information), which is conducive to the realization of high-performance PeLEDs.[63] The optoelectronic properties of the target device (P123 3 mg ml^{-1}, annealing 1 min) and the control device (P123 0 mg ml^{-1}, annealing 10 min) were further compared. We evaluated the impact of the introduction of P123 in PeLEDs based on the changes in the optoelectronic characteristics of the devices, including current density, luminance, CE, and EQE. The specific parameters of the devices are shown in Table S3 (Supporting Information). The current density–voltage–luminance (J–V–L) curve (Figure 4b) shows that the addition of P123 does not significantly change the current density after the device is turned on, but reduces the leakage current, which further indicates the passivation effect of P123 on the perovskite films. Compared with the pristine PeLED (6210 cd m^{-2}), the maximum luminance of the target device is increased to 10 200 cd m^{-2}. The CE-V and EQE-V characteristics of the device are shown in Figure 4c,d, respectively. The maximum CE of 42.4 cd A^{-1} and the maximum EQE of 14.45% are achieved in the target PeLED, which is significantly higher than the 6.93 cd A^{-1} and 2.3% of the pristine device. In addition, the spectral stability of target PeLED was also tested. As shown in Figure 4e, when the bias voltage of the device was increased from 3.0 to 6.0 V, the EL peak did not shift, indicating that the device has good spectral stability. It shows that the all-inorganic perovskite grains added via P123 are very stable in the electric field. When P123 was added, the EL peak blue shifts from 517 to 514 nm, and the FWHM slightly increases from 20.1 to 20.9 nm (Figure S9a, Supporting Information), which are consistent with PL spectra (Figure 3a). As shown in Figure 4f, the EL spectrum of the device is located at (0.25, 0.45) in Commission Internationale de I'Eclairage (CIE). We demonstrated good reproducibility of the devices by counting the EQE of 20 devices (Figure S9b, Supporting Information). At the same time, we tested the device lifetime (Figure S9c, Supporting Information). Compared with the pristine device (2 min), the lifetime of the target device (29 min) was greatly improved, but overall, the lifetime is still needed to be prolonged. We attribute the large amount of Joule heat generated during the operation of the device led to the decomposition of organic matter, which can be verified from the AFM image of Figure S5 (Supporting Information).

Subsequently, the flexible PeLED with the same structure was fabricated on the PEN substrate (**Figure 5**a). The J–V–L and CE–V–EQE characteristics of the device are shown in Figure 5b,c, respectively. The target flexible PeLED has a maximum luminance of 3390 cd m^{-2}, a maximum CE of 39.2 cd A^{-1}, and a maximum EQE of 11.9%. The EL peak of flexible PeLED was located at 516 nm (Figure 5d), and after folding 1000 cycles with a bending radius of 4.45 mm and a strain of 2.2%, the luminance and

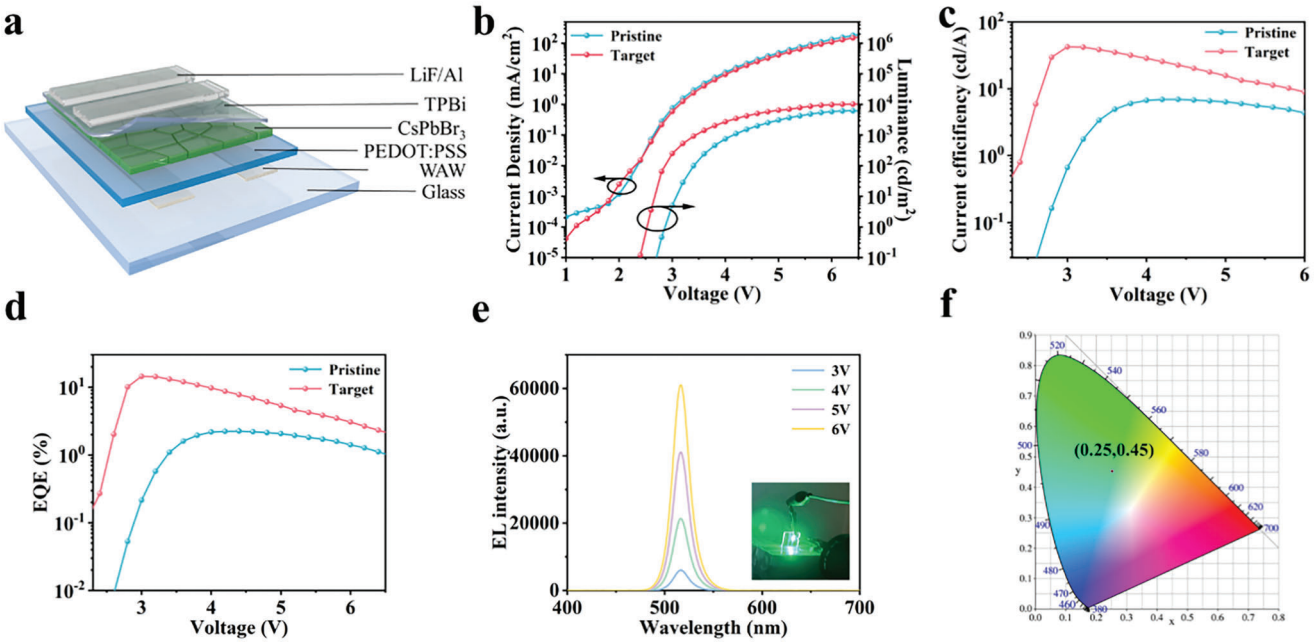

Figure 4. Structure and EL performance of PeLED. a) Schematic representation of the PeLED. b) *J*–*V*–*L*, c) CE-V, and d) EQE-V characteristics of PeLED. e) EL spectra of PeLEDs under different voltage bias. f) Commission Internationale de l'Eclairage (CIE) coordinates of the PeLED.

CE of the pristine device were reduced to 13.78% and 55.19% of the initial state, respectively. While the device using ITO electrode and P123-modified was reduced to 0.57% and 0.27% of the initial state. The target device still maintains 55.56% luminance and 96.5% CE compared to the initial values. SEM (Figures S10 and S11, Supporting Information) shows that WAW electrode have better bending stability than ITO electrode, and the introduction of P123 leads to uniform distribution of small-sized grains, thus greatly improving the flexibility of PeLED. Finally, we summarize the performance parameters of flexible PeLED in Table S4 (Supporting Information).[64] This is one of the best-performing devices among the all-inorganic flexible PeLEDs reported so far. These results put forward a feasible guidance in designing electrode and choosing appropriate additives for high performance flexible all-inorganic green PeLED.

3. Conclusion

In summary, we have demonstrated an effective strategy to improve the optoelectronic performance of flexible PeLED by employing a new ITO-free transparent electrode WAW, which is more favorable for flexible PeLEDs. At the same time, the additive P123 is added to the perovskite precursor solution to optimize the crystallization kinetics and recombination kinetics. The nucleation and crystallization process ends in a very short time (1 min) to obtain uniform distributed small-size grains. In addition, the OH– and C–O functional groups in P123 can be used to anchor the crystal structure of perovskite and repair the non-radiative recombination center. These synergistic effects lead to highly efficient green PeLED with a maximum luminance of 10 200 cd m^{-2} and an EQE of 14.45%, and spectrally stabilized EL emission at 516 nm. At the same time, the prepared flexible PeLED has a maximum luminance of 3390 cd m^{-2} and an EQE of 11.9%. And thanks to the excellent bending resistance of WAW electrode and the small grain size of perovskites induced by P123, the flexible PeLED keeps a luminance of 55.56% and a current efficiency of 96.5% of its original value, respectively, after bending 1000 cycles. This study reveals rational electrodes and additive engineering for improving the performance of all-inorganic green PeLED, and provides a feasible strategy for the preparation of efficient flexible PeLED.

4. Experimental Section

Materials and Chemicals: PEDOT:PSS and TPBI were purchased from Xi'an Polymer Light Technology Company, CsBr was purchased from Kanto Chemical Company, $PbBr_2$ was purchased from Liaoning Preferred New Energy Technology Company, Au and Al were purchased from Zhong Nuo Advanced Material(Beijing)Technology Co., Ltd. P123 were purchased from Innochem.

Perovskite Precursor Preparation: The pristine perovskite precursor solutions were prepared by dissolving CsBr and $PbBr_2$ (molar ratio of 1.71:1) in DMSO solvent. For the modified perovskite precursors, P1213 was added into the solution for defect passivation. The concentrations of P123 in DMSO were 3 mg mL^{-1}, respectively. All the precursor solutions were stirred in a nitrogen-filled glovebox at room temperature for at least 48 h before use.

WO_3/Au/WO_3 Electrode Fabrication: Patterned WAW electrodes were deposited on the precleaned glass or PEN substrates by electron beam evaporation through shadow masks. WO_3 (35 nm), Au (6, 8, 10, 15 nm), and WO_3 (35 nm) were deposited sequentially at room temperature by electron beam evaporation. The evaporation rates of WO_3 and Au were 0.1 and 0.5 nm s^{-1}, respectively.

Device Fabrication Processes: The device structure of perovskite light-emitting diode mainly includes the following sections: WO_3/Au/WO_3/PEDOT: PSS /$CsPbBr_3$/ TPBi/LiF/Al. The PEDOT: PSS solution were deposited onto the WAW substrate via onestep spin-coating at 2500 rpm for 40 s. The substrate was then placed on a 140 °C hot plate

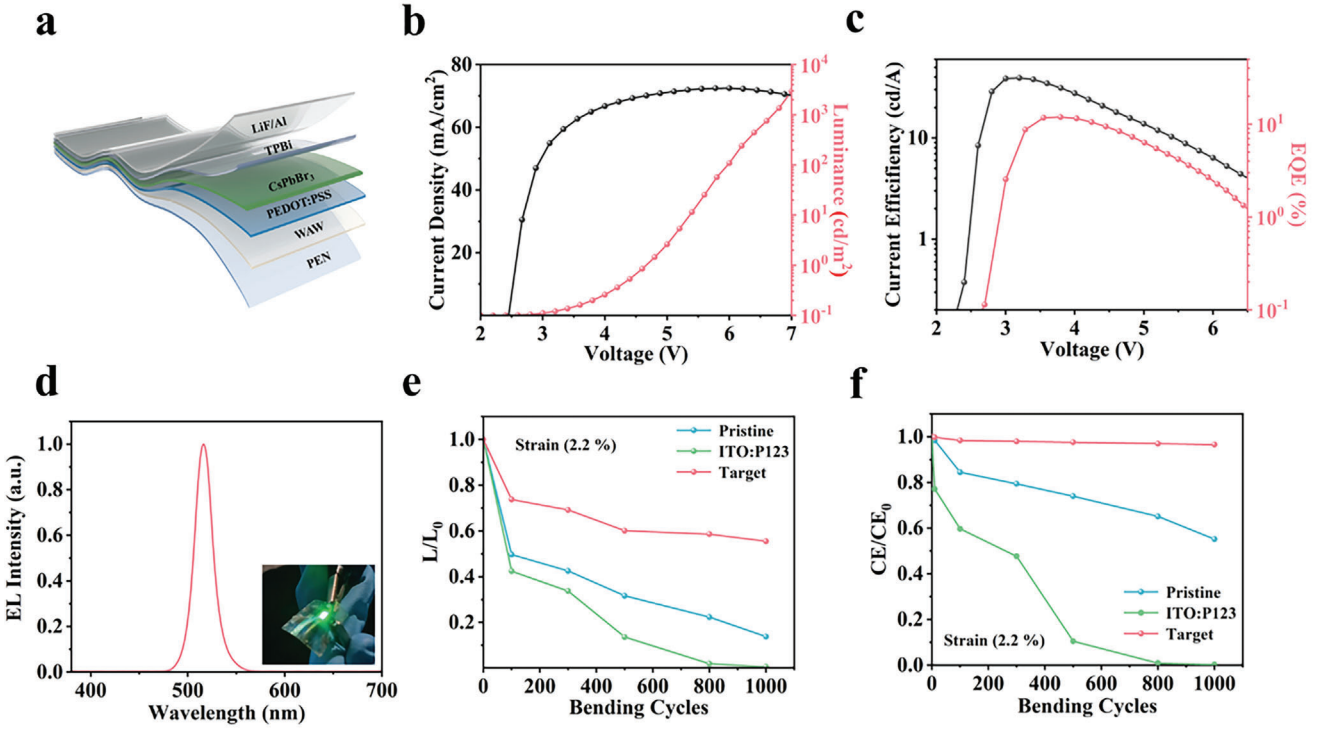

Figure 5. a) Schematic representation of the flexible PeLED. b) *J*–*V*–*L*, c) CE-V-EQE. d) EL curves of the flexible PeLED. e) Luminance and f) CE of the flexible PeLED under repeated bending cycles.

for 10 min. Then, the substrates were transferred to a glove box filled with nitrogen, and the perovskite films were deposited via spin-coating at 4500 rpm for 60 s and heated at 70 °C for 1 min. Finally, TPBI (30 nm), LiF (1 nm), and Al (80 nm) were sequentially deposited using a vacuum coater under a vacuum of less than 4×10^{-4} Pa.

Thin Film and Device Characterizations: SEM (Hitachi S4800) and AFM (Shimadzu SPA9700) were used to characterize the surface morphology of the perovskite films. XRD spectra of the perovskite films were collected using a powder diffraction device (Bruker Advance D8-ray). The absorption spectra of the perovskite films were measured using an ultraviolet-visible spectrophotometer (Shimadzu UV-3101 PC). Steady-state PL spectra of the perovskite films were measured using a Hitachi F-7000 fluorescence spectrometer. XPS were measured using a Thermo Scientific NEXSA instrument. The current density– voltage curves and luminance–voltage curves of the device were measured using a Keithley 2611 digital source meter and a luminance meter (Konica-Minolta LS-110). PLQY and TRPL tests were carried out using an FLS920 steady-state/transient fluorescence spectrometer. The FTIR measurement was conducted by using absorption infrared spectrometer (Thermo Fisher Nicolet Is 5). The impedance spectra were measured under a small AC signal with an amplitude of 5.0 mV at a DC voltage of 3.0 V (Agilent 4294 A).

The Bending Test and the Stability Experiment: Put the flexible perovskite light-emitting diode into the flexible material bending tester for bending, and use the bending stress (ϵ) to express the force of the device:

$$\varepsilon = \frac{D}{2R} \tag{7}$$

where D is the overall thickness of the flexible PeLED, and R is the bending radius. The EL performance parameters of the device at the voltage corresponding to the maximum CE have been measured after different bending cycles, and the variation trends of luminance and CE with bending times were recorded.

Supporting Information

Supporting Information is available from the Wiley Online Library or from the author.

Acknowledgements

K.S. and Z.B. contributed equally to this work. This work was supported by Jilin Province Science and Technology Research Project No. 20230101366JC, 20220201091GX;National Natural Science Foundation of China Nos. 62175235, 51973208, 62035013, and 61975256; and the Project supported by the Dawn Talent Training Program of CIOMP.

Conflict of Interest

The authors declare no conflict of interest.

Data Availability Statement

The data that support the findings of this study are available from the corresponding author upon reasonable request.

Keywords

all-inorganic, crystallization regulation, defect passivation, flexible perovskite light-emitting diodes, transparent electrodes

Received: July 21, 2023
Revised: September 11, 2023
Published online: October 27, 2023

[1] S. Sun, P. Jia, M. Lu, P. Lu, Y. Gao, Y. Zhong, C. Tang, Y. Zhang, Z. Wu, J. Zhu, Y. Zhang, W. W. Yu, X. Bai, *Adv. Funct. Mater.* **2022**, *32*, 2204286.
[2] Y.-H. Kim, H. Cho, T.-W. Lee, *Proc. Natl. Acad. Sci. USA* **2016**, *113*, 11694.
[3] X.-K. Liu, W. Xu, S. Bai, Y. Jin, J. Wang, R. H. Friend, F. Gao, *Nat. Mater.* **2021**, *20*, 10.
[4] J. J. Yoo, G. Seo, M. R. Chua, T. G. Park, Y. Lu, F. Rotermund, Y.-K. Kim, C. S. Moon, N. J. Jeon, J.-P. Correa-Baena, V. Bulovic, S. S. Shin, M. G. Bawendi, J. Seo, *Nature* **2021**, *590*, 587.
[5] C. H. Kang, I. Dursun, G. Liu, L. Sinatra, X. Sun, M. Kong, J. Pan, P. Maity, E.-N. Ooi, T. K. Ng, *Light: Sci. Appl.* **2019**, *8*, 94.
[6] H. Cho, S.-H. Jeong, M.-H. Park, Y.-H. Kim, C. Wolf, C.-L. Lee, J. H. Heo, A. Sadhanala, N. Myoung, S. Yoo, S. H. Im, R. H. Friend, T.-W. Lee, *Science* **2015**, *350*, 1222.
[7] Z. Liu, W. Qiu, X. Peng, G. Sun, X. Liu, D. Liu, Z. Li, F. He, C. Shen, Q. Gu, F. Ma, H.-L. Yip, L. Hou, Z. Qi, S.-J. Su, *Adv. Mater.* **2021**, *33*, 2103268.
[8] P. You, G. Tang, J. Cao, D. Shen, T.-W. Ng, Z. Hawash, N. Wang, C.-K. Liu, W. Lu, Q. Tai, *Light: Sci. Appl.* **2021**, *10*, 68.
[9] H. Chen, H. Wang, J. Wu, F. Wang, T. Zhang, Y. Wang, D. Liu, S. Li, R. V. Penty, I. H. White, *Nano Res.* **2020**, *13*, 1997.
[10] K.-G. Lim, T.-H. Han, T.-W. Lee, *Energy Environ. Sci.* **2021**, *14*, 2009.
[11] Y. Fang, Q. Dong, Y. Shao, Y. Yuan, J. Huang, *Nat. Photonics* **2015**, *9*, 679.
[12] Y. Rakita, S. R. Cohen, N. K. Kedem, G. Hodes, D. Cahen, *MRS Commun.* **2015**, *5*, 623.
[13] Z. Yuan, Y. Miao, Z. Hu, W. Xu, C. Kuang, K. Pan, P. Liu, J. Lai, B. Sun, J. Wang, S. Bai, F. Gao, *Nat. Commun.* **2019**, *10*, 2818.
[14] S. G. R. Bade, J. Li, X. Shan, Y. Ling, Y. Tian, T. Dilbeck, T. Besara, T. Geske, H. Gao, B. Ma, K. Hanson, T. Siegrist, C. Xu, Z. Yu, *ACS Nano* **2016**, *10*, 1795.
[15] S.-Y. Chou, R. Ma, Y. Li, F. Zhao, K. Tong, Z. Yu, Q. Pei, *ACS Nano* **2017**, *11*, 11368.
[16] T.-H. Kim, C.-S. Lee, S. Kim, J. Hur, S. Lee, K. W. Shin, Y.-Z. Yoon, M. K. Choi, J. Yang, D.-H. Kim, T. Hyeon, S. Park, S. Hwang, *ACS Nano* **2017**, *11*, 5992.
[17] W. Zheng, R. Lin, Z. Zhang, Q. Liao, J. Liu, F. Huang, *Nanoscale* **2017**, *9*, 12718.
[18] J. C. Yu, D. B. Kim, E. D. Jung, B. R. Lee, M. H. Song, *Nanoscale* **2016**, *8*, 7036.
[19] J. Wang, N. Wang, Y. Jin, J. Si, Z.-K. Tan, H. Du, L. Cheng, X. Dai, S. Bai, H. He, Z. Ye, M. L. Lai, R. H. Friend, W. Huang, *Adv. Mater.* **2015**, *27*, 2311.
[20] J. C. Yu, J. H. Park, S. Y. Lee, M. H. Song, *Nanoscale* **2019**, *11*, 1505.
[21] K. Ellmer, *Nat. Photonics* **2012**, *6*, 809.
[22] O. Inganäs, *Nat. Photonics* **2011**, *5*, 201.
[23] A. Kumar, C. Zhou, *ACS Nano* **2010**, *4*, 11.
[24] C. G. Granqvist, *Sol. Energy Mater. Sol. Cells* **2007**, *91*, 1529.
[25] T. Hada, K. Wasa, S. Hayakawa, *Thin. Solid. Films* **1971**, *7*, 135.
[26] H.-K. Seo, H. Kim, J. Lee, M.-H. Park, S.-H. Jeong, Y.-H. Kim, S.-J. Kwon, T.-H. Han, S. Yoo, T.-W. Lee, *Adv. Mater.* **2017**, *29*, 1605587.
[27] J.-Y. Lee, S. T. Connor, Y. Cui, P. Peumans, *Nano Lett.* **2008**, *8*, 689.
[28] J. Han, S. Yuan, L. Liu, X. Qiu, H. Gong, X. Yang, C. Li, Y. Hao, B. Cao, *J. Mater. Chem. A* **2015**, *3*, 5375.
[29] J. E. Yoo, K. S. Lee, A. Garcia, J. Tarver, E. D. Gomez, K. Baldwin, Y. Sun, H. Meng, T.-Q. Nguyen, Y.-L. Loo, *Proc. Natl. Acad. Sci. USA* **2010**, *107*, 5712.
[30] P. Avouris, C. Dimitrakopoulos, *Mater. Today* **2012**, *15*, 86.
[31] Y. Lee, S. Bae, H. Jang, S. Jang, S.-E. Zhu, S. H. Sim, Y. I. Song, B. H. Hong, J.-H. Ahn, *Nano Lett.* **2010**, *10*, 490.
[32] J.-H. Park, K.-J. Ahn, K.-I. Park, S.-I. Na, H.-K. Kim, *J. Phys. D: Appl. Phys.* **2010**, *43*, 115101.
[33] J. C. Bernède, Y. Berredjem, L. Cattin, M. Morsli, *Appl. Phys. Lett.* **2008**, *92*, 62.
[34] K. Schulze, B. Maennig, K. Leo, Y. Tomita, C. May, J. Hüpkes, E. Brier, E. Reinold, P. Bäuerle, *Appl. Phys. Lett.* **2007**, *91*, 073521.
[35] L. Kinner, T. Dimopoulos, G. Ligorio, E. J. W. List-Kratochvil, F. Hermerschmidt, *RSC Adv.* **2021**, *11*, 17324.
[36] W. Ji, T. Wang, B. Zhu, H. Zhang, R. Wang, D. Zhang, L. Chen, Q. Yang, H. Zhang, *J. Mater. Chem. C* **2017**, *5*, 4543.
[37] A. Manekkathodi, B. Chen, J. Kim, S.-W. Baek, B. Scheffel, Y. Hou, O. Ouellette, M. I. Saidaminov, O. Voznyy, V. E. Madhavan, A. Belaidi, S. Ashhab, E. Sargent, *J. Mater. Chem. A* **2019**, *7*, 26020.
[38] J. Liang, X. Guo, L. Song, J. Lin, Y. Hu, N. Zhang, X. Liu, *Appl. Phys. Lett.* **2017**, 111.
[39] H. Wu, Y. Zhang, X. Zhang, M. Lu, C. Sun, X. Bai, T. Zhang, G. Sun, W. W. Yu, *Adv. Electron. Mater.* **2018**, *4*, 1700285.
[40] C. Xie, X. Zhao, E. W. Y. Ong, Z.-K. Tan, *Nat. Commun.* **2020**, *11*, 4213.
[41] J. C. Yu, A.-Y. Lee, D. B. Kim, E. D. Jung, D. W. Kim, M. H. Song, *Adv. Mater. Technol.* **2017**, *2*, 1700003.
[42] C. Chen, T.-H. Han, S. Tan, J. Xue, Y. Zhao, Y. Liu, H. Wang, W. Hu, C. Bao, M. Mazzeo, R. Wang, Y. Duan, Y. Yang, *Nano Lett.* **2020**, *20*, 4673.
[43] B. Han, S. Yuan, T. Fang, F. Zhang, Z. Shi, J. Song, *ACS Appl. Mater. Interfaces* **2020**, *12*, 14224.
[44] H. Wu, Y. Zhang, M. Lu, X. Zhang, C. Sun, T. Zhang, V. L. Colvin, W. W. Yu, *Nanoscale* **2018**, *10*, 4173.
[45] L. Song, X. Guo, Y. Hu, Y. Lv, J. Lin, Z. Liu, Y. Fan, X. Liu, *J. Phys. Chem. Lett.* **2017**, *8*, 4148.
[46] X. Liu, X. Guo, Y. Lv, Y. Hu, Y. Fan, J. Lin, X. Liu, X. Liu, *Adv. Opt. Mater.* **2018**, *6*, 1801245.
[47] Y.-l. Su, J. Wang, H.-z. Liu, *J. Colloid Interface Sci.* **2002**, *251*, 417.
[48] Y.-R. Shi, K.-L. Wang, Y.-H. Lou, D.-B. Zhang, C.-H. Chen, J. Chen, Y.-X. Ni, S. Öz, Z.-K. Wang, L.-S. Liao, *Nano Energy* **2022**, *97*, 107200.
[49] B. Wang, Y.-H. Zhou, S. Yuan, Y.-H. Lou, K.-L. Wang, Y. Xia, C.-H. Chen, J. Chen, Y.-R. Shi, Z.-K. Wang, L.-S. Liao, *Angew. Chem., Int. Ed.* **2023**, *62*, e202219255.
[50] R. Sun, Q. Tian, M. Li, H. Wang, J. Chang, W. Xu, Z. Li, Y. Pan, F. Wang, T. Qin, *Adv. Funct. Mater.* **2023**, *33*, 2210071.
[51] H. Hu, M. Singh, X. Wan, J. Tang, C.-W. Chu, G. Li, *J. Mater. Chem. A* **2020**, *8*, 1578.
[52] Y. Li, Z. Chen, B. Yu, S. Tan, Y. Cui, H. Wu, Y. Luo, J. Shi, D. Li, Q. Meng, *Joule* **2022**, *6*, 676.
[53] C. Bi, S. V. Kershaw, A. L. Rogach, J. Tian, *Adv. Funct. Mater.* **2019**, *29*, 1902446.
[54] Q. Jiang, Z. Chu, P. Wang, X. Yang, H. Liu, Y. Wang, Z. Yin, J. Wu, X. Zhang, J. You, *Adv. Mater.* **2017**, *29*, 1703852.
[55] Y. Shao, Z. Xiao, C. Bi, Y. Yuan, J. Huang, *Nat. Commun.* **2014**, *5*, 5784.
[56] Z. Liang, S. Zhao, Z. Xu, B. Qiao, P. Song, D. Gao, X. Xu, *ACS Appl. Mater. Interfaces* **2016**, *8*, 28824.
[57] J. Yang, S. Xiong, T. Qu, Y. Zhang, X. He, X. Guo, Q. Zhao, S. Braun, J. Chen, J. Xu, *ACS Appl. Mater. Interfaces* **2019**, *11*, 13491.
[58] Q. Dong, Y. Fang, Y. Shao, P. Mulligan, J. Qiu, L. Cao, J. Huang, *Science* **2015**, *347*, 967.
[59] W. Zhou, Y. Shen, L.-X. Cao, Y. Lu, Y.-Y. Tang, K. Zhang, H. Ren, F.-M. Xie, Y.-Q. Li, J.-X. Tang, *Adv. Funct. Mater.* **2023**, 2301425.
[60] L. Zhou, M. Yan, G. Luo, L. Xu, Y. Fang, D. Yang, *Adv. Funct. Mater.* **2023**, 2303370.
[61] W. Xiong, C. Zou, W. Tang, S. Xing, Z. Wang, B. Zhao, D. Di, *ACS Energy Lett.* **2023**, *8*, 2897.
[62] S. Yuan, Z.-K. Wang, M.-P. Zhuo, Q.-S. Tian, Y. Jin, L.-S. Liao, *ACS Nano* **2018**, *12*, 9541.
[63] X. Liu, X. Guo, Z. Gan, N. Zhang, X. Liu, *J. Phys. Chem. C* **2016**, *120*, 26703.
[64] J.-T. Wang, S.-Z. Wang, Y.-H. Zhou, Y.-H. Lou, Z.-K. Wang, *Sci. China Mater.* **2023**, *66*, 1.